HAL open science

Parametric Instability of an Axially Moving Belt Subjected to Multifrequency Excitations: Experiments and Analytical Validation

Guilhem Michon, Lionel Manin, Didier Remond, Régis Dufour, Robert Parker

To cite this version:

Guilhem Michon, Lionel Manin, Didier Remond, Régis Dufour, Robert Parker. Parametric Instability of an Axially Moving Belt Subjected to Multifrequency Excitations: Experiments and Analytical Validation. Journal of Applied Mechanics, 2008, 75 (4), pp.1-8. 10.1115/1.2910891 . hal-02117137

HAL Id: hal-02117137

https://hal.science/hal-02117137v1

Submitted on 6 May 2019

HAL is a multi-disciplinary open access archive for the deposit and dissemination of scientific research documents, whether they are published or not. The documents may come from teaching and research institutions in France or abroad, or from public or private research centers.

L'archive ouverte pluridisciplinaire **HAL**, est destinée au dépôt et à la diffusion de documents scientifiques de niveau recherche, publiés ou non, émanant des établissements d'enseignement et de recherche français ou étrangers, des laboratoires publics ou privés.

Distributed under a Creative Commons Attribution - NonCommercial 4.0 International License

Parametric Instability of an Axially Moving Belt Subjected to Multifrequency Excitations: Experiments and Analytical Validation

Guilhem Michon
Université de Toulouse, ISAE DMSM, 10 Avenue Edouard Belin, 31055 Toulouse, France

Lionel Manin, Didier Remond, Regis Dufour
LaMCoS, INSA-Lyon, CNRS UMR5259, F69621, France

Robert G. Parker
Department of Mechanical Engineering, The Ohio State University, 650 Ackerman Road, Columbus, OH 43202

This paper experimentally investigates the parametric instability of an industrial axially moving belt subjected to multifrequency excitation. Based on the equations of motion, an analytical perturbation analysis is achieved to identify instabilities. The second part deals with an experimental setup that subjects a moving belt to multifrequency paramet-ric excitation. A data acquisition technique using optical encoders and based on the angular sampling method is used with success for the first time on a nonsynchronous belt transmission. Transmission error between pulleys, pulley/belt slip, and tension fluctuation are deduced from pulley rotation angle measurements. Experimental results validate the theoretical analysis. Of particular note is that the instability regions are shifted to lower frequencies than the classical ones due to the multifrequency excitation. This experiment also demonstrates nonuniform belt characteristics (longitudinal stiffness and friction co-efficient) along the belt length that are unexpected sources of excitation. These variations are shown to be sources of parametric instability.

Keywords: automotive belt, parametric instabilities, multifrequency excitation, experi-mental investigation, angular sampling

1 Introduction

Instead of classical V belts, serpentine drives are used in front end accessory drives (FEADs). They use flat and multiribbed belts running over multiple accessory pulleys, leading to simplified assembly and replacement, longer belt life, and compactness [1]. Numerous mechanical phenomena occur in this application: rotational vibrations [2], hysteretic behavior of belt tensioner [3], nonlinear transverse vibration due to the existence of pulley eccentricity [4], dry friction tensioner behavior [5], or parametric excitation.

Commonly known under the category of axially moving media, belt spans are subjected to parametric excitation from their operating environment as studied by Zhang [6]. A theoretical nonlinear dynamic analysis is also analyzed by Mockenstrum et al. [7,8]. However, only Pellicano et al. [9,10] present a coupled theoretical and experimental investigation, where the excitation comes from pulley eccentricity, which causes simultaneous direct and parametric excitation.

Widely used in automotive engines, belt spans experience multifrequency excitation caused by engine firing and accessory variable torques [11]. Belt parametric instability occurs as transverse vibration in these applications, where the problems are noise and belt fatigue.

This paper builds on a previous work of Parker and Lin [12] as an experimental illustration and model validation. First, it deals with the general moving belt model subjected to multifrequency tension and speed fluctuations. Then a specific test bench is presented, which produce this kind of excitation. Data acquisition is based on the principle of pulse timing method and leads to angular sampling for frequency analysis [13]. This method is applied here for the first time on a nondiscrete geometry. The theoretical results from perturbation analysis are compared to the experimental ones. An unexpected source of parametric excitation is also highlighted.

2 Mathematical Model

A mathematical model of an axially moving beam subjected to multifrequency tension and speed parametric excitation is used to establish the parametric instability region transition curves. The equation of motion for transverse vibration of a beam of length L moving with time dependent transport velocity $c(T)$ is governed by [14]

$$\rho A(V_{,TT} + c_{,T}V_{,X} + 2cV_{,TX} + c^2V_{,XX}) - (P_s + P_d(T))V_{,XX} + EIV_{,XXXX} = 0 \tag{1}$$

where ρA is the mass per unit length, EI the bending stiffness, V the transverse displacement, P_s the mean belt tension, $P_d(T)$ the dynamic tension, and T and X the independent time and spatial variables. The dynamic tension results from longitudinal motion of the endpoints as a result of pulley oscillations and quasistatic midplane stretching from transverse deflection, and is given by

$$P_d(T) = \frac{EA}{L}\left[U(L,T) - U(0,T) + \frac{1}{2}\int_0^L V_{,X}^2 dX\right] \tag{2}$$

EA is the longitudinal stiffness modulus and U the longitudinal displacement. With the dimensionless parameters,

$$x, v, u = \frac{X, V, U}{L}, \quad t = T\sqrt{\frac{P_s}{\rho A L^2}}, \quad \gamma = c \Big/ \sqrt{\frac{P_s}{\rho A}}$$

$$\zeta = \frac{EA}{P_s}, \quad \mu = \frac{EI}{P_s L^2}, \quad \Omega_i = \sqrt{\frac{\rho A L^2}{P_s}}\tilde{\Omega}_i \tag{3}$$

Equation (1) becomes

$$v_{,tt} + 2\gamma v_{,tx} + \gamma_{,t} v_{,x} - (1-\gamma^2) v_{,xx} + \mu v_{,xxxx} - \zeta\left[u(1,t) - u(0,t) + \frac{1}{2}\int_0^1 v_{,x}^2 dx\right] v_{,xx} = 0 \tag{4}$$

The belt tension and speed fluctuations are, respectively,

$$\zeta[u(1,t) - u(0,t)] = \sum_{i=1}^{k} \varepsilon_i \cos(\Omega_i t + \theta_i) \tag{5}$$

$$\gamma = \gamma_0 + \sum_{i=1}^{k'} \varepsilon_i' \cos(\Omega_i' t + \theta_i') \tag{6}$$

where $\varepsilon_i = EAu_i/P_s < 1$ represents the ratio of the ith spectral component of the dynamic tension fluctuation to the mean span tension.

As investigated in Ref. [12], the boundaries of the instability regions can be obtained on the basis of Floquet theory and perturbation analysis.

Linearizing Eq. (4) and writing in state-space form gives [12]

$$AW_t + BW + \sum_{i=1}^{k'} \varepsilon_i' \{\sin(\Omega_i' t + \theta_i') C + \Omega_i' \cos(\Omega_i' t + \theta_i') D\} W - \sum_{i=1}^{k} \varepsilon_i \cos(\Omega_i t + \theta_i) EW + \left(\sum_{i=1}^{k'} \varepsilon_i' \sin(\Omega_i' t + \theta_i')\right)^2 EW = 0 \tag{7}$$

where

$$A = \begin{bmatrix} 1 & 0 \\ 0 & -(1-\gamma_0^2)\frac{\partial^2}{\partial x^2} + \alpha \frac{\partial^4}{\partial x^4} \end{bmatrix},$$

$$B = \begin{bmatrix} 2\gamma_0 \frac{\partial}{\partial x} & -(1-\gamma_0^2)\frac{\partial^2}{\partial x^2} + \alpha \frac{\partial^4}{\partial x^4} \\ (1-\gamma_0^2)\frac{\partial^2}{\partial x^2} - \alpha \frac{\partial^4}{\partial x^4} & 0 \end{bmatrix}$$

$$C = \begin{bmatrix} 2\frac{\partial}{\partial x} & 2\gamma_0 \frac{\partial^2}{\partial x^2} \\ 0 & 0 \end{bmatrix}, \quad D = \begin{bmatrix} 0 & \frac{\partial}{\partial x} \\ 0 & 0 \end{bmatrix}, \quad E = \begin{bmatrix} 0 & \frac{\partial^2}{\partial x^2} \\ 0 & 0 \end{bmatrix},$$

$$W = \begin{bmatrix} v_{,t} \\ v \end{bmatrix} \tag{8}$$

The inner product in the state space is $\langle W, V\rangle = \int_0^1 W^T \bar{V} dx$, where overbar denotes the complex conjugate and superscript T denotes the transpose. The Galerkin basis consists of the state-space eigenfunctions of the nonparametrically excited moving string ($\mu=0$) system [15]

$$\Phi_n = \begin{bmatrix} j\omega_n \psi_n \\ \psi_n \end{bmatrix} = \begin{bmatrix} \lambda_n \psi_n \\ \psi_n \end{bmatrix} \tag{9}$$

where ψ_n are the complex eigenfunctions of Eq. (4) and ω_n the natural frequencies

$$\psi_n = \frac{1}{n\pi\sqrt{1-\gamma_0^2}} e^{jn\pi\gamma_0 x} \sin(n\pi x), \quad \lambda_n = jn\pi(1-\gamma_0^2) \tag{10}$$

Let us define $E_{nm} = \langle E\Phi_n, \Phi_m\rangle$ and $E_{\bar{n}m} = \langle E\bar{\Phi}_n, \Phi_m\rangle$, with similar relations for the C and D operators.

Using perturbation analysis to consider speed and tension fluctuations, primary instability occurs when

$$\Omega_l = \Omega_l' = 2\omega_n \pm \sqrt{(\varepsilon_l'|-jC_{\bar{n}n} + 2\omega_n D_{\bar{n}n}|)^2 + (\varepsilon_l|E_{\bar{n}n}|)^2} - |E_{\bar{n}n}|^2 \times \left[-\sum_{i=1, i\neq l}^{k} \varepsilon_i^2 \frac{2\omega_n}{\Omega_i^2 - 4\omega_n^2} + \frac{\varepsilon_l^2}{8\omega_n}\right] - |-jC_{\bar{n}n} + 2\omega_n D_{\bar{n}n}|^2 \times \left[-\sum_{i=1, i\neq l}^{k'} \varepsilon_i'^2 \frac{2\omega_n}{\Omega_i'^2 - 4\omega_n^2} + \frac{\varepsilon_l^2}{8\omega_n}\right] + \sum_{i=1}^{k'} \left(\frac{\varepsilon_i'}{2}\right)^2 |E_{nn}| \tag{11}$$

and secondary instability occurs when

$$\Omega_l = \Omega_l' = \omega_n \pm \sqrt{\left(\frac{\varepsilon_l^2}{\omega_n}\mathrm{Im}(E_{nn})|E_{\bar{n}n}|\right)^2 \left(\frac{\varepsilon_l'^2}{\omega_n}\mathrm{Im}(-jC_{nn} + \omega_n D_{nn})|-jC_{\bar{n}n} + \omega_n D_{\bar{n}n}|\right)^2} - |E_{\bar{n}n}|^2 \left[-\sum_{i=1, i\neq l}^{k} \varepsilon_i^2 \frac{\omega_n}{\Omega_i^2 - 4\omega_n^2} + \frac{\varepsilon_l^2}{3\omega_n}\right] - |-jC_{\bar{n}n} + \omega_n D_{\bar{n}n}|^2 \left[-\sum_{i=1, i\neq l}^{k'} \varepsilon_i'^2 \frac{\omega_n}{\Omega_i'^2 - 4\omega_n^2} + \frac{\varepsilon_l^2}{3\omega_n}\right] + \sum_{i=1}^{k'} \left(\frac{\varepsilon_i'}{2}\right)^2 |E_{nn}| \tag{12}$$

3 Experimental Setup

In industrial applications, excitation sources are not at a single frequency, especially in an automotive engine. Engine firing and driven accessories cause multifrequency speed and tension fluctuations. Furthermore, practical belt speeds are such that they impact the dynamics and must be included. The following experiment examines parametric instabilities from this kind of excitation in a moving belt system.

3.1 Belt Drive Description. The studied transmission consists of four pulleys linked together by an automotive multiribbed belt, as shown in Fig. 1. The input shaft speed (from 0 rpm to 2000 rpm) is controlled by a 60 kW electric motor. The driven shaft is connected to a hydraulic pump. The output pressure of the fluid is controlled to apply a mean torque on the driven pulley. Due to its design, however, the pump generates torque fluctuations of order 2 (i.e., 2 pulses/rev) around the mean value. These fluctuations cause tension variations that parametrically excite the moving belt.

Due to the rotation direction, the upper span is tight and the lower one is slack. As these two spans have approximately the same length, the instability will appear in the slack span for the lowest excitation frequencies. Figure 2 shows an example of transverse vibration of the lower span.

3.2 Measurement Devices. Angular positions are measured by optical encoders mounted on Pulleys 1, 2, and 3 (respectively,

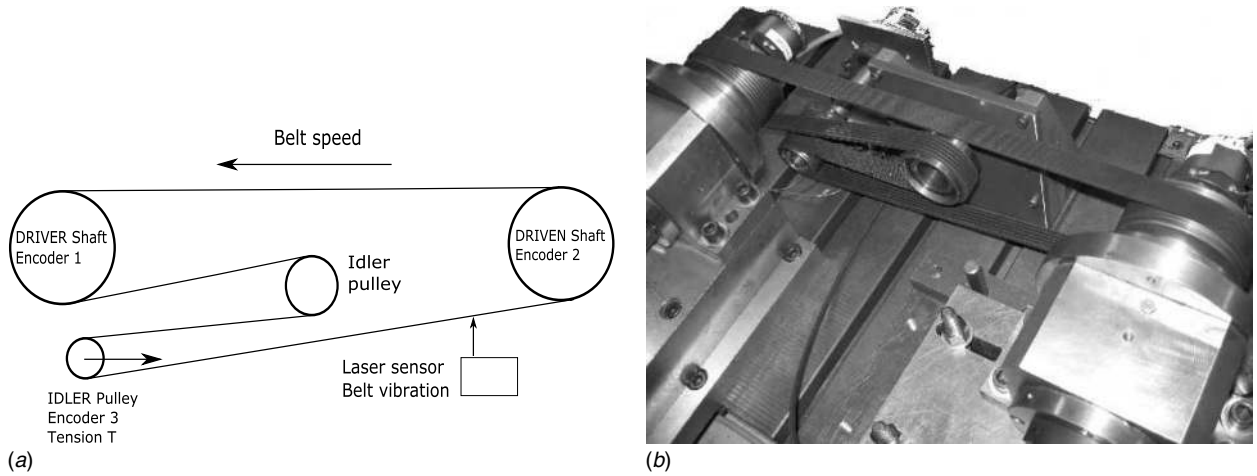

Fig. 1 Experimental setup for parametrically excited moving belt drive

2048 pulses/rev, 2048 pulses/rev, and 2500 pulses/rev). Belt tension is measured by a piezoelectric sensor on the Pulley 3 support and belt lateral vibration by a laser displacement sensor (0.02 m range, 10 μm dynamic resolution).

The data acquisition system is custom made with a PXI frame including classical data acquisition boards and a four-channel counterboard permitting the use of the pulse timing method. Each optical encoder delivers a square signal (TTL) as it rotates. Between two rising edges of this signal, a counter records the number of pulses given by a high frequency clock (80 MHz), see Fig. 3. For each encoder, it is therefore possible to build a time vector that contains the times of occurence of the TTL signal's rising edges. Hence, the total rotation angle of each shaft is determined and instantaneous rotation speed and acceleration are deduced. In this application, measurement is triggered on the reference encoder mounted on the driving shaft and analog signals are acquired at each instant of the reference encoder's rising edge. Obviously, when an analog signal is sampled in the angular domain, the speed conditions are taken into account in order to set the cutoff frequency of antialiasing filters. An important characteristic of this measurement principle is to separate resolution and precision. Resolution is given by the number of pulses/rev, and the theoretical angular precision is proportional to the ratio between rotation speed and counterclock frequency. The grating quality of the optical encoder disk, as well as the electronic signal conditioning and processing, may also affect the practical accuracy.

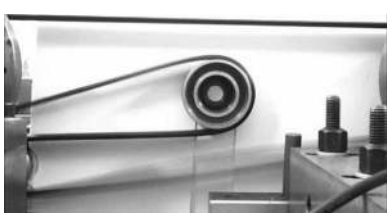

Fig. 2 Example of instability in slack belt span

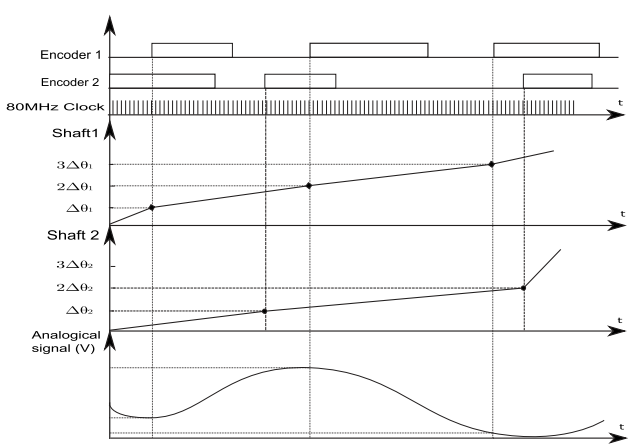

Fig. 3 Angular sampling principle

3.3 Angular Sampling Benefits. Compared to classical acquisition [16], data are resampled based on the angular rotation of a chosen encoder, which is not necessarily the reference one. It consists in calculating the angular rotations of the other encoders at the times corresponding to the rising edges of the sampling encoder. Hence, if angular sampling is performed on encoder i, the angular positions of each of the slave encoders are computed from linear interpolation at the times corresponding to the encoder i rising edge locations, see Fig. 4(a).

For the analog signals, the same method is applied and they are recorded at the angular frequency of the reference encoder. This method is called angular sampling and is detailed in Ref. [13]. It is mainly applied in rotating machines with synchronous transmission elements, such as gears or timing belts. Its application to a transmission in the presence of belt slip is novel and provides important advantages as described below. This technique is especially useful for systems with variable speed because the position of the sampling points and the angular resolution remain exactly the same when the speed fluctuates.

As the angular sampling frequency is constant based on the encoder resolution, instead of performing the fast Fourier transform (FFT) analysis in the time domain, this is performed in the angular domain. In other words, the measured signals are treated as functions of the angular position of the sampling encoder. The sampling encoder's position plays the role typically filled by time in classical FFT analysis.

The spectral data are a function of angular frequency, which has units of rad^{-1}. The maximum angular frequency is $1/\delta\theta$, where $\delta\theta = 2\pi/N_g$ is the angular resolution of the sampling encoder based on N_g gratings. Increments on the angular frequency axis are spaced at $\delta f = 1/N\delta\theta$, where N is the number of sampling encoder rising edges in the collected data. Examples of classical Campbell and angular frequency diagrams are compared in Fig. 5. On Fig. 5(a), natural frequencies are located at a constant frequency when speed increases while speed-dependent frequency orders linearly increase. In the angular frequency domain, however, natural frequencies appear as hyperbola ($f = \omega(1/\theta)$) and

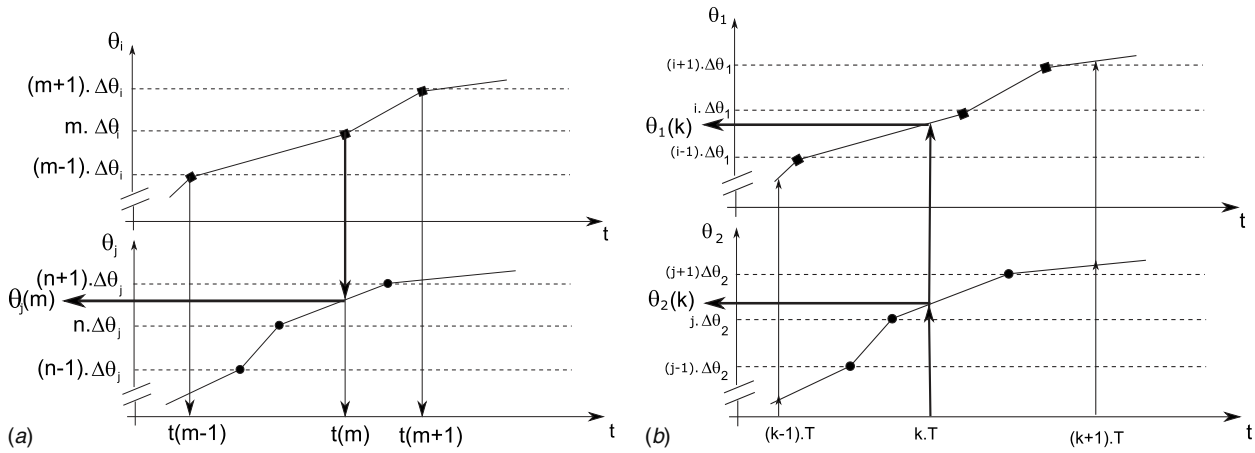

Fig. 4 Angular resampling method (*a*) and time resampling method (*b*)

speed-dependent frequency orders are located at a constant angular frequency ($f=a\cdot\omega$ leads to $1/\theta=a$), vertical lines parallel to the speed axis, see Fig. 5(*b*).

Thus, the main advantages of performing angular sampling in this application are as follows:

- Sampling points are exactly located in reference to the geometry of the rotating machine, even when speed varies. It permits to compare several measurement results based on the same sampling conditions.
- Spectral analysis is always performed with the same accuracy and the same resolution. Angular sampling also ensures that the magnitude of harmonic components are exactly estimated [13].
- By choosing Encoder 3 as reference, and assuming that no slip occurs between belt and the idler pulley since no torque is being transmitted, the sampling points are attached to the belt.

  Therefore, it is more convenient to identify speed-dependent frequency components on a graph with an angular frequency axis related to a chosen reference encoder.

For standard Fourier analysis, it is necessary to get the measurements as a function of one single time vector with equally spaced intervals. This requires a time resampling of the data using linear interpolation, as shown in Fig. 4(*b*).

3.4 Phase Difference Measurement. This angular sampling method has already been used for many synchronous transmission studies (gearbox, timing belt drive) but never for nonsynchronous transmissions, such as serpentine multiribbed belt drives. The transmission error ϵ is defined as the angular rotation difference between shaft i and shaft j,

$$\epsilon = \theta_i - \eta\cdot\theta_j \tag{13}$$

where η and $\theta_{i,j}$ are, respectively, the transmission ratio and the angular positions of shaft i, j.

In the case of nonsynchronous belt drive systems, some creep occurs between the belt and the pulleys due to the power transmission by friction [17,18]. Indeed, the creep corresponds to the relative slip between the belt and the driven pulley as the belt elongates on the pulley contact arc as its tension increases. Here, the transmission error between Pulleys 3 and 2 is considered.

The rotation of Pulley 3 is not totally transmitted to Pulley 2 due to the belt stretching on Pulley 2, which causes a delay. Therefore, the mean value of the transmission error is not zero as it is for a synchronous drive, but rather always increases (Fig. 6). In our application, analysis permits decomposition of the observed transmission error as the sum of a linear function of time representing the transmission error due to the pulley belt creep ϵ_{creep}, and the residual transmission error ϵ_{res} due to the system dynamic as in synchronous transmission.

$$\epsilon = \theta_3 - \eta\cdot\theta_2 = \epsilon_{\text{res}} + \epsilon_{\text{creep}} \tag{14}$$

where ϵ_{creep} is identified from ϵ as a linear regression of time assuming a constant mean rotation speed. Removing the linear part ϵ_{creep} from the transmission error ϵ yields the zero-mean pe-

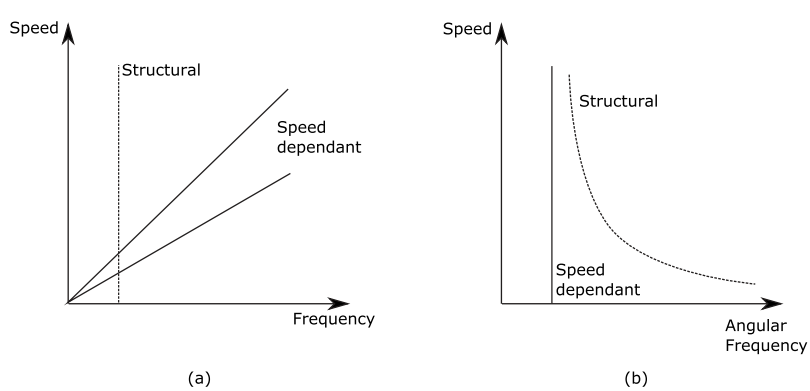

Fig. 5 Campbell diagrams in (*a*) time and (*b*) angular frequency domain

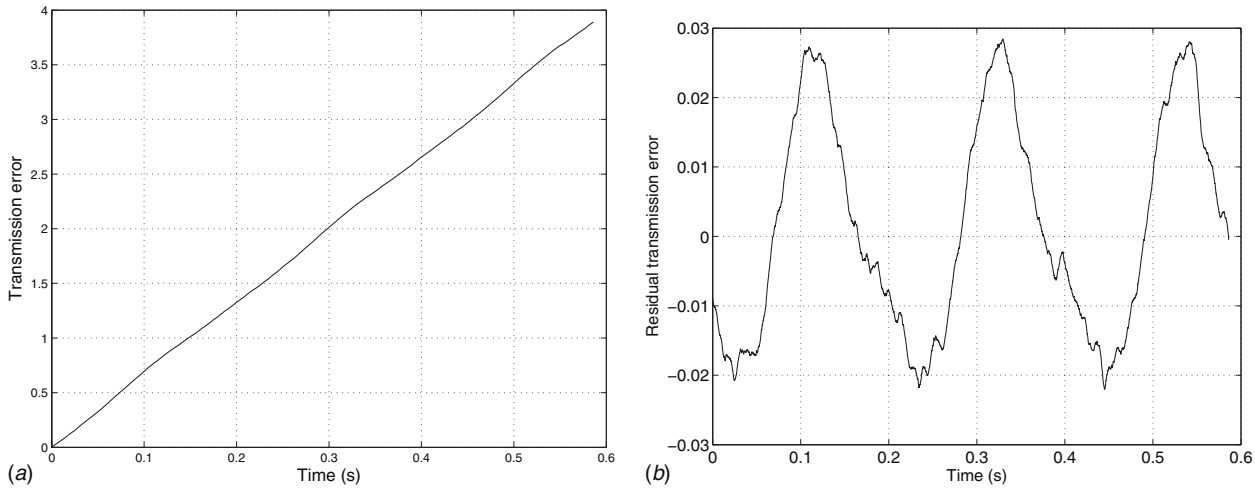

Fig. 6 Total (*a*) and residual (*b*) transmission error versus time

riodic residual transmission error ϵ_{res} (Fig. 6).

As mentioned in the theoretical model description, the dynamic belt tension can be expressed as the difference of the endpoint positions and midplane stretching from transverse vibration, see Eq. (2). Considering the belt span that connects Pulleys 3 and 2, and taking into account the belt translation direction, $U(L,T)$ and $U(0,T)$ correspond, respectively, to the belt unseating point on Pulley 3 and to the belt seating point on Pulley 2. These two points are not fixed in space since pulley rotations oscillate around the linearly increasing angles w_3t and w_2t. Assuming a no-slip condition at these two points, $U(L,T)$ and $U(0,T)$ can be estimated from pulley angle oscillations multiplied by the respective pulley pitch radius. Finally, the difference between $U(L,T)$ and $U(0,T)$ corresponds to the residual transmission error at time T. Therefore, residual transmission error and belt tension fluctuation are related. Figure 7 presents the measured progression of belt tension and residual transmission error angular waterfall analysis with change in rotation speed (note that all waterfall plots are top views). The same frequency components appear on each graph and prove that the measurement system with optical encoders and angular sampling permits evaluation of belt tension fluctuation. Finally, this analysis shows that the transmission error includes the pulley belt creep plus the system dynamic.

3.5 Nonuniform Belt Characteristic Identification and Consequences. The low modulation observed on the dynamic transmission error (Fig. 6) corresponds to the belt traveling frequency and demonstrates that there are nonuniform belt characteristics. In order to check this nonuniformity, a belt has been cut in ten equal parts. Each part has been tested to determine longitudinal rigidity modulus k and damping C. Each belt sample is clamped at one end and has a mass m suspended at the other, see Fig. 8. This system is excited via a shock hammer. The free response is recorded via an accelerometer and postprocessed to ob-

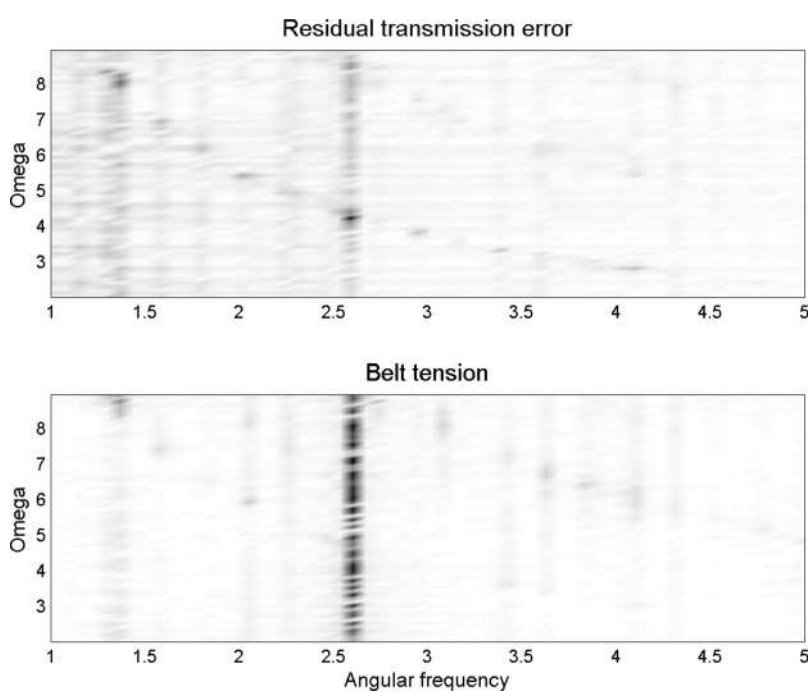

Fig. 7 Belt tension and transmission error angular top-view waterfall as a function of rotation speed

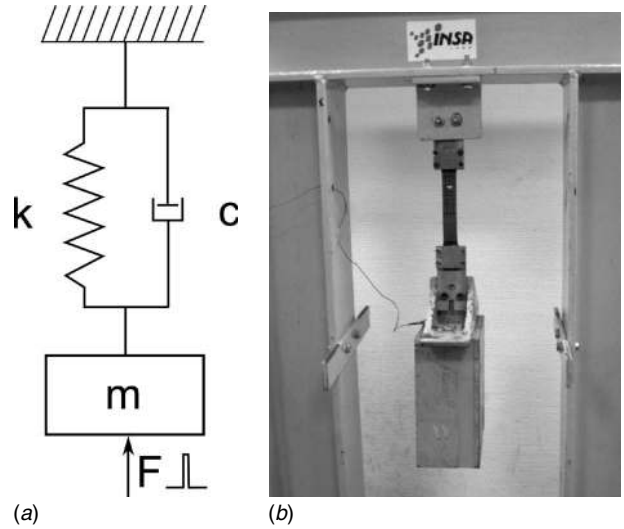

Fig. 8 Experimental setup for the local belt characteristics identification

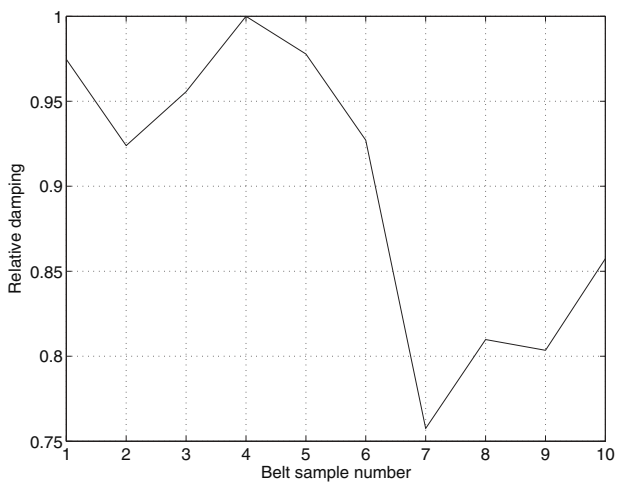

Fig. 9 Dimensionless damping evolution along the belt length C_i/C_{max}

tain belt longitudinal stiffness and damping. Longitudinal damping coefficients of belt samples, normed by the maximum measured value, are plotted versus belt sample number in Fig. 9. Non-negligible variation is observed for C while local stiffness, and therefore EA, is constant. This irregularity is probably due to the manufacturing process (printing, cord winding, cutting). The low frequency modulation observed is shown to be a parametric excitation source next.

4 Belt Span Instability Analysis

4.1 Experimental Investigation. On the global experimental setup for a given initial belt tension and mean torque, a speed sweep of the driving shaft is performed from 532 rpm to 1512 rpm in 14 rpm increments (70 tests). The experimental results are presented in Fig. 10 as a top-view waterfall in the angular frequency domain for (*a*) the transverse vibration, (*b*) belt tension, and (*c*) belt speed. All parameters are dimensionless as defined in Sec. 2 (waterfall FFT in the time-frequency domain are given in Appendix).

The belt tension angular waterfall, Fig. 10(*b*), exhibits lines parallel to the speed axis, which proves a speed-dependent excitation. The belt transverse vibration angular waterfall is presented on Fig. 10(*a*). The instabilities are represented by the black spots located on a hyperbola. which proves parametric instability. The system is unstable for numerous frequencies.

4.2 Main Instability Regions. The main excitation of the system comes from the pump design, which creates torque fluctuations of order 2, inducing speed and tension fluctuations. Regarding belt instability, speed variation is a negligible source of excitation compared to the tension fluctuation. The latter is observed to be the principle source of parametric excitation and is located on the angular frequency waterfall graph at abscissa 2.60 as a vertical line. Primary and secondary instability regions, circled on Fig. 10(*a*), are the response to this torque excitation.

Experimentally, the primary instability occurs for $\Omega_1 \in [7.9, 8.8]$. This region is classically wider than the corresponding secondary region (which occurs for $\Omega_1 \in [4.1, 4.5]$), but also shifted of 0.3 from $2\omega_1$ toward lower frequencies due to the multifrequency excitation.

Considering the small transverse rigidity modulus and the large span length in this application, the bending stiffness modulus is neglected. Therefore, in the following, the belt span is considered as a string ($\mu=0$). Thus, using Eqs. (7) and (8) and $C_{\bar{n}n}=(1-e^{-2jn\pi\gamma_0})/2$, $D_{\bar{n}n}=0$, $E_{\bar{n}n}=(1-e^{-2jn\pi\gamma_0})/(4\gamma_0)$, and $E_{nn}=jn\pi(1+\gamma_0^2)/2$. The experimental parameters introduced in the model are $\gamma_0=0.5$, $\omega_1=4.3$, $\Omega_2=8$, $\Omega_2'=8$, $\varepsilon_1'=0.001$, $\varepsilon_2=0.3$, $\varepsilon_2'=0.001$. For $\varepsilon_1=0.7$, the instability region occurs for $\Omega_1 \in [7.8\ 9.2]$.

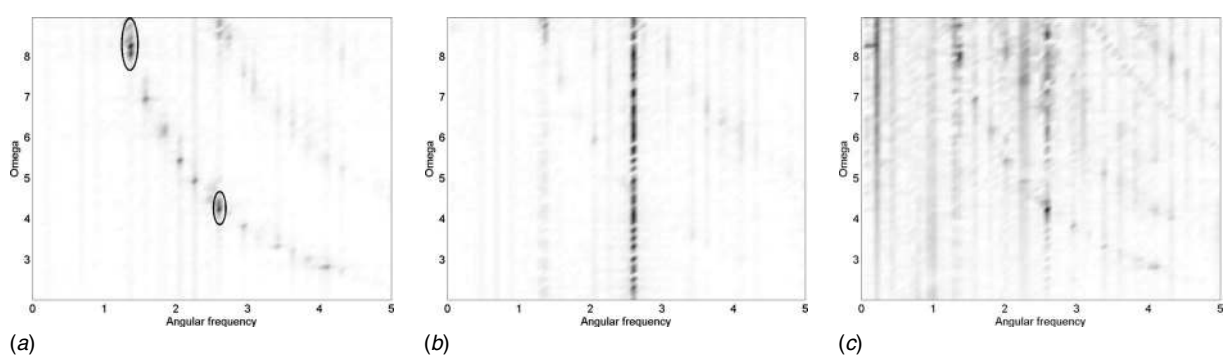

Fig. 10 Experimental angular top-view waterfall: (*a*) transverse vibration, (*b*) belt tension fluctuation, (*c*) belt speed fluctuation

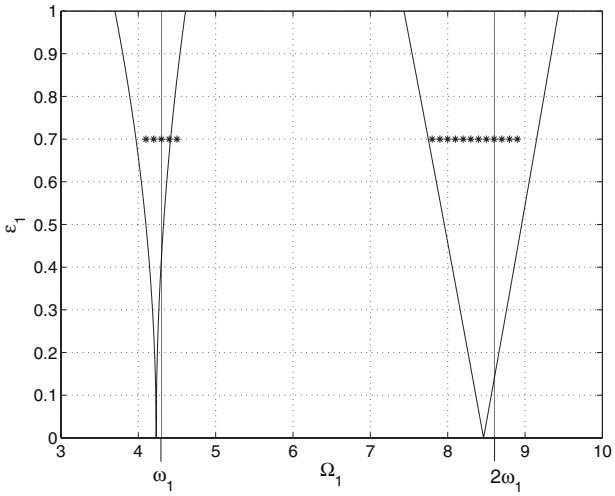

Fig. 11 Instability region. Model (solid line) and experiment (stars).

analysis is presented and permits to validate theoretical instabilities. The main conclusion are as follows:

- Parametric instabilities occur in experimental system such as belt drive.
- Measurement system based on angular sampling is shown to be an efficient tool for instability analysis in belt drive systems.
- Irregular belt characteristics have been detected and highlighted as unexpected source of parametric excitation.
- Instability regions are shifted when subjected to multifrequency excitation.
- Experimental observations confirm the theoretical results.

Further analysis will focus on the role of the hysteretic behavior of the belt tensioners on these instabilities.

Appendix

Figure 12 represents the top-view waterfall in the classical Campbell-like diagram.

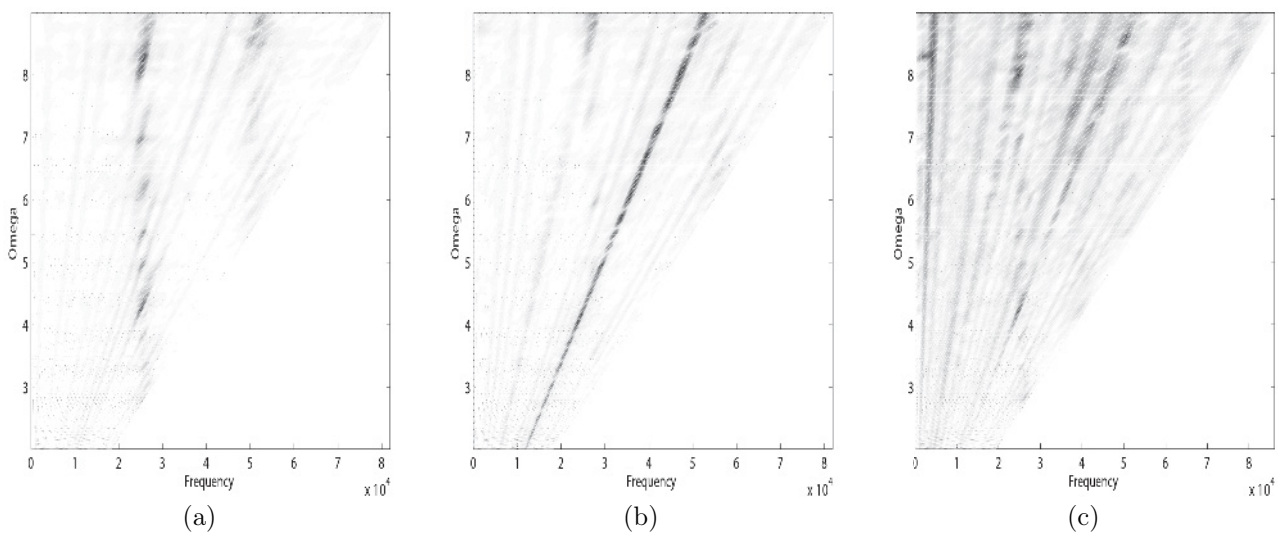

Fig. 12 Experimental classical Campbell-like diagram top-view waterfall: transverse vibration (*a*), belt tension fluctuation (*b*), belt speed fluctuation (*c*)

The instability region boundaries are plotted as a function of the excitation amplitude ε_1 in Fig. 11. When $\Omega_2 < 2\omega_1$, the second source of excitation shift the instability region to lower frequencies. While this phenomenon is not classical, the experimental observations confirm the theoretical results of Ref. [12].

4.3 Low Amplitude Instability Region. The low frequency modulation observed on the residual transmission error due to the belt characteristic irregularity highlighted in Sec. 3.5 is a source of parametric excitation. It appears on the waterfall plot of the tension fluctuation as low level parallel lines separated by 0.20, that is, the belt traveling frequency. This irregularity explains the peripheral instabilities presented on Fig. 10(*a*).

5 Conclusion

This paper focuses on an experimental investigation of an industrial axially moving belt subjected to multifrequency excitation. Comparison with analytical results from a perturbation

References

[1] Gerbert, G., 1981, "Some Notes on V-Belt Drives," ASME J. Mech. Des., **103**, pp. 8–18.

[2] Hwang, S. J., Perkins, N. C., Ulsoy, A., and Meckstroth, R. J., 1994, "Rotational Response and Slip Prediction of Serpentine Belt Dirve Systems," ASME J. Vibr. Acoust., **116**, pp. 71–78.

[3] Michon, G., Manin, L., and Dufour, R., 2005, "Hysteretic Behavior of a Belt Tensioner, Modeling and Experimental Investigation," J. Vib. Control, **11**(9), pp. 1147–1158.

[4] Wickert, J. A., 1992, "Non-Linear Vibration of a Traveling Tensioned Beam," Int. J. Non-Linear Mech., **27**(3), pp. 503–517.

[5] Leamy, M. J., and Perkins, N. C., 1998, "Nonlinear Periodic Response of Engine Accessory Drives With Dry Friction Tensioners," ASME J. Vibr. Acoust., **120**, pp. 909–916.

[6] Zhang, L., and Zu, J. W., 1999, "One-to-One Auto-Parametric Resonance in Serpentine Belt Drive Systems," J. Sound Vib., **232**, pp. 783–806.

[7] Mockensturm, E., Perkins, N., and Ulsoy, A., 1996, "Stability and Limit Cycles of Parametrically Excited, Axially Moving Strings," ASME J. Vibr. Acoust., **118**, pp. 346–351.

[8] Mockensturm, E. and Guo, J., 2005, "Nonlinear Vibration of Parametrically Excited Viscoelastic Axially Moving Media," ASME J. Appl. Mech., **72**, pp. 374–380.

[9] Pellicano, F., Catellani, G., and Fregolent, A., 2004, "Parametric Instability of Belts, Theory and Experiments," Comput. Struct., **82**, pp. 81–91.

[10] Pellicano, F., Fregolent, A., Bertuzzi, A., and Vestroni, F., 2001, "Primary and Parametric Non-Linear Resonances of a Power Transmission Belt: Experimental and Theoretical Analysis," J. Sound Vib., **244**, pp. 669–684.

[11] Cheng, G., and Zu, J. W., 2003, "Nonstick and Stick-Slip Motion of a Coulomb-Damped Belt Drive System Subjected to Multifrequency Excitations," ASME J. Appl. Mech., **70**, pp. 871–884.

[12] Parker, R., and Lin, Y., 2001, "Parametric Instability of Axially Moving Media Subjected to Multifrequency Tension and Speed Fluctuation," ASME J. Appl. Mech., **68**, pp. 49–57.

[13] Remond, D., and Mahfoudh, J., 2005, "From Transmission Error Measurements to Angular Sampling in Rotating Machines With Discrete Geometry," Shock Vib., **9**, pp. 1–13.

[14] Thurman, A. L., and Mote, C. D., Jr., 1969, "Free, Periodic, Non-Linear Oscillation of an Axially Moving String," ASME J. Appl. Mech., **36**, pp. 83–91.

[15] Jha, R., and Parker, R., 2000, "Spatial Discretization of Axially Moving Media Vibration Problems," ASME J. Vibr. Acoust., **122**, pp. 290–294.

[16] Houser, D. R., and Blankenshio, G. W., 1989, "Methods for Measuring Transmission Error Under Load and at Operating Speeds," SAE Trans., **98**(6), pp. 1367–1374.

[17] Gerbert, G., and Sorge, F., 2002, "Full Sliding Adhesive-Like Contact of V-Belts," ASME J. Mech. Des., **124**, pp. 706–712.

[18] Betchel, S. E., Vohra, S., Jacob, K. I., and Carslon, C. D., 2000, "The Stretching and Slipping of Belts and Fibers on Pulleys," ASME J. Appl. Mech., **67**, pp. 197–206.